ISSN (e): 2250 – 3005 || Volume, 08 || Issue, 2|| February – 2018 ||
International Journal of Computational Engineering Research (IJCER)

Study of Geometric Variations on Drag over Rectangular Cavities at Yaw

Dhaval Shiyani[1], Peter J. Disimile[2]
[1] Graduate student, University of Cincinnati, Cincinnati, OH 45220
[2] Associate Professor, University of Cincinnati, Cincinnati, OH 45220
Corresponding author: Dhaval Shiyani (shiyandr@mail.uc.edu)

Abstract:
The impact of varying L/D and L/W ratios, of clean rectangular cavities immersed within a turbulent boundary layer and placed at yaw is studied. Specifically, the cavity behavior, drag in particular, is examined in this work. Steady state simulations were performed to develop an improved understanding of the effect of *L*, *D*, and *W* variations on the drag generated by these cavities. Simulations were performed using OpenFOAM, the open source CFD package. Five *L/D* ratios, namely 8.125, 12, 24, 32.5, and 64, are considered along with three *L/W* ratios, namely 8.125, 16.25, and 32. All of the *L/D* and *L/W* ratio cavities are yawed at angles of 0^0, 30^0, 45^0, 60^0, 75^0, and 90^0. The drag produced by each of the cavities are then plotted against the yaw angles. A change is cavity behavior is observed as the *L/D* and *L/W* ratios are varied. The change in flow phenomena due to the yaw angle variation was previously studied by the author in [1].

Keywords: *Cavity, Drag, Yaw, Computational Fluid Dynamics (CFD), OpenFOAM, Geometric variation*, L/D, L/W

Nomenclature:

Parameter	Definition	Units
L	Length of cavity	mm
D	Depth of Cavity	mm
W	Width of Cavity	mm
L_{ip}	Incoming plate length	m
L_{ep}	Exit plate length	m
V_d	Domain height	m
x	Longitudinal direction	
y	Vertical direction	
z	Transverse direction	
p	Pressure	Pa
ρ	Density	kg/m^3
P	p/ρ	Pa m^3/kg
U_∞	Freestream Velocity	m/s
U	Local Mean Velocity	m/s
φ	Yaw angle	^{0}, degrees
C_d	Coefficient of Drag	-
C_{d_max}	Maximum coefficient of drag for a given geometry	-
L/D	Length to Depth ratio	-
L/W	Length to Width ratio	-
δ	Boundary layer thickness	mm
δ^*	Displacement layer thickness	mm
θ	Momentum layer thickness	mm
H	Shape Factor	-
k	Turbulent kinetic energy	m^2/s^2
ε	Turbulent dissipation rate	m^2/s^3
ω	Specific rate of dissipation	1/s
y^+	Dimensionless wall distance	-

I. INTRODUCTION

Study of drag characteristics of a rectangular cavity has been a topic of interest for aircraft development, automobile development and areas where major surface cutouts are part of the design. The topic has been studied extensively over the past 80 years, beginning with Krishnamurthy [18] and onto Rossiter [3] with their early studies on the effect of surface cutouts in high speed turbulent flows. Following that, majority of research in this area has been focused on noise generation and its suppression techniques, particularly for high speed flows. Recent computational studies try to validate experimental findings in the SPL levels generated by cavities using DNS, LES and URANS methods.

However, the drag generated by such surface irregularities has been largely overlooked, with a few experimental investigations [2][3][4][5][6][7][10][11][12][18] and fewer computational studies [13]. Especially in the cases of yawed cavities, where the cavity goes through changes in flow type [1]. The drag caused by depressions and cutouts for a commercial aircraft can reach as high as 3% of the total drag [5]. The effect of yaw angle variation on drag generated in cavities immersed in fully developed turbulent flows was previously reported by the author [1].

The current study focuses on the effect of documenting fundamental geometric parameters of the cavity, namely *L/D* and *L/W* ratios, coupled with the effect of yaw angle on the drag produced by the cavity. To this end, three dimensional CFD simulations using OpenFOAM were conducted on a varying rectangular cavity geometry immersed in a turbulent boundary layer. Each set of simulations has a fixed *L/D* and *L/W* ratio while the yaw angle was varied in six steps of 0^0, 30^0, 45^0, 60^0, 75^0 and 90^0. The value of C_d, a result of the viscous and turbulent stresses coupled with the pressure drag component, was obtained for the cavity faces along with the pressure profiles at each yaw angle. The geometry was then varied in two ways; varying the *D* with the *L* and *W* fixed changing the *L/D* ratio and varying the *W* with the *L* and *D* fixed resulting in *L/W* ratio variations.

The cavity dimensions, with the orientation in the 0^0 configuration, can be seen in figure 1. The rotation of the cavity is clockwise such that at φ of 0^0 the major axis of the cavity is perpendicular to the incoming flow and becomes tangential at φ of 90^0. Figure 1 also shows the domain dimensions which are detailed in section 3.1.

The *L/D* and *L/W* ratios studied in the current investigation are detailed in table 1. All the *L/D* and *L/W* ratios mentioned in this study are the effective *L/D* and *L/W* ratios at an φ of 90^0, since the ratio changes with φ

	At φ 0^0		**At φ 90^0**	
	L/D	***L/W***	***L/D***	***L/W***
***L/D* variation**	1	0.123	8.125	16.25
	1.477	0.123	12	16.25
	2.95	0.123	24	16.25
	4	0.123	32	16.25
	8	0.123	64	16.25
***L/W* variation**	2	0.123	16.25	8.125
	1	0.062	16.25	16.25
	0.25	0.015	16.25	65

Table 1. Geometric variations for the current study

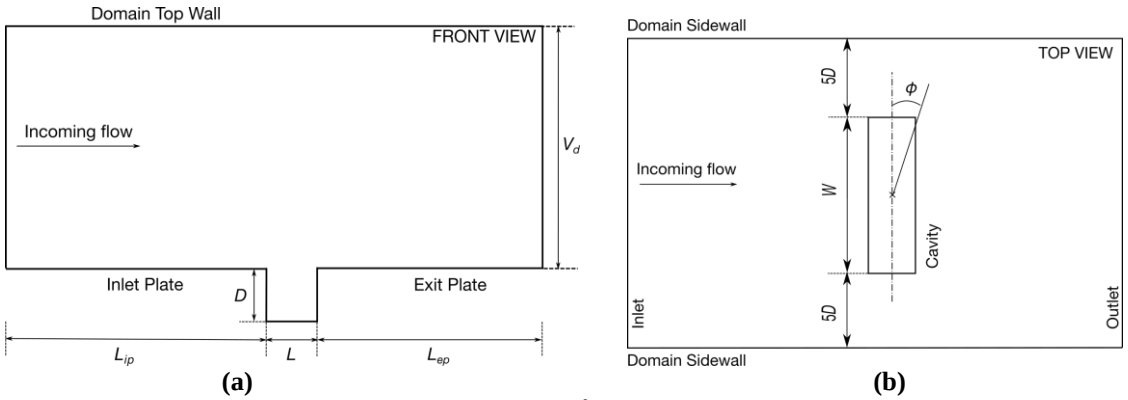

(a) **(b)**

Figure 1. Cavity and Domain dimensions at φ 0^0 (a) Front View (b) Top View (Not to scale)

1.1 Background

There are three basic classifications of cavity flows, open type, closed type, and transitional type (see Fig. 2). The flow is deemed open when the separating shear layer from the leading edge impinges on the trailing edge without contact on any other cavity faces while closed flows describe a shear layer separating off the leading edge which impinges and attaches on the cavity floor, then separating off the floor to continue towards the trailing edge. A transitional type of cavity flow describes the state of transition of flow between open and closed types, when the shear layer neither impinges directly on the trailing edge or on the cavity floor.

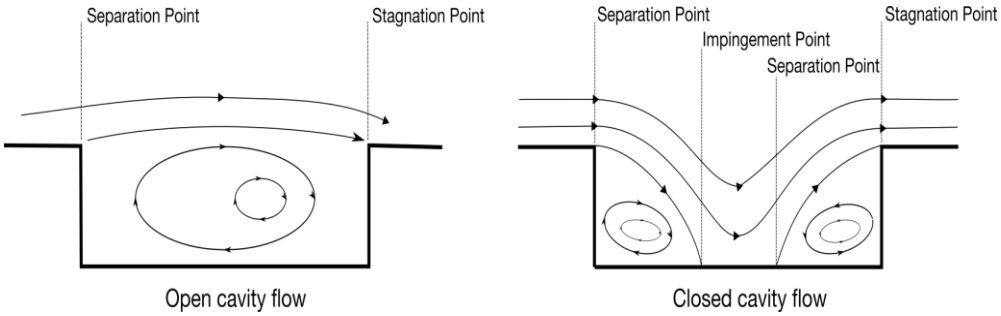

Figure 2. Classification of Cavity flows [1]

Classification of cavity flow is also dependent on the Length/Depth (*L/D*) and the Length/Width (*L*/*W*) ratios of the cavities [1]. Since the current study involves multiple *L/D* and *L/W* ratios which when yawed would change the effective *L/D* and *L/W* ratio, the flow type varies from open to close.

Another classification of cavity flows is shallow and deep type. Cavities with *L/D* ratios greater than 1 are termed shallow cavities and the ones with *L/D* ratios less than 1 are termed deep cavities. The cavities studied in this investigation go through both shallow and deep type depending on the geometry and orientation.

II. COMPUTATIONAL METHOD

2.1. Numerical method

The Semi-Implicit Method for Pressure-Linked Equations, known as SIMPLE, is used to solve the steady-state problem which iteratively solves the Navier-Stokes (NS) equations (eqns. 1 and 2). The time terms are dropped from the equations due to the steady nature of the simulations. Temperature variations is not in the scope of this study leading to the energy equation not being solved.

An OpenFOAM solver [17], called simpleFoam, provides solution to incompressible, turbulent flows using the SIMPLE algorithm and hence is the choice of solver for this investigation.

$$\nabla \cdot \left(\rho \vec{U}\right) = 0 \tag{1}$$

$$\nabla \cdot (\vec{V}\vec{V}) - \nabla \cdot (\nu \nabla \vec{V}) = -\nabla p \tag{2}$$

The generalized goemtric-algebriac multi-grid solver (GAMG) is used to compute the pressure term whereas the velocity and turbulence parameters, k and ε, are solved using the smooth solver with a GaussSeidel smoother specified for all solvers. The divergence and gradient terms are computed using second order Gaussian integration.

2.2. Domain

The domain dimensions with the cavity immersed can be seen in figure 1. The domain and cavity dimensions were chosen based on previous research by the author [1]. To ensure similar freestream conditions and incoming boundary layer for all geometries studied, the inlet plate length L_{ip}, the exit plate length L_{ep} and the domain height V_d are kept constant. The incoming boundary layer is developed over an inlet flat plate with the length, Lip and the details of which are provided in section 2.4. An exit flat plate of length, L_{ep}, was used to ensure the flow dissipates into the free stream after interacting with the cavity and minimizes the effects of the exit domain wall on the cavity flow.

To negate the effect of domain side walls on the cavity flow field, the cavity and the domain side walls were separated by a side-plate of width 5*D* on either side of the cavity, as seen in figure 1. The width of the side plate was parameterized with the depth and changes with geometric change since using a fixed side wall width leads to side walls boundaries too close to the cavity boundaries in very low *L/W* studies. Analyzing the results (section 3) it is evident that the effects of domain boundaries on the cavity flow field has been minimized with the chosen domain dimensions.

2.3. Boundary conditions and Convergence:

A velocity of 25 m/s is prescribed at the inlet, using the velocity inlet boundary condition, whereas the outlet uses a pressure outlet boundary condition which prescribes the pressure value, *P*, of 82,714.3 Pa m^3/kg. No slip wall boundary conditions are used for the inlet plate, exit plate, the cavity faces and the domain side walls. And a symmetry boundary condition is used on the domain top wall.

The SIMPLE algorithm has a reputation for slow convergence in some cases [19], the numerical scheme and solver parameters used in this investigation lead to a fast and smooth convergence of the solution. The residuals for velocity, pressure and turbulence variables was monitored with a threshold of 1e-04 set for convergence. The mass equation was monitored as well to ensure a stable solution.

Though the solution reached a converged state at different rates and with slightly different behavior for various *L/D* and *L/W* ratios and yaw variation.

2.4. Incoming boundary layer

An incoming flat plate of length, 0.4 m was used to develop a boundary layer of thickness 10.20 mm before interaction with the cavity leading edge. The parameters for the boundary layer presented were calculated 1mm upstream of the cavity leading edge with a freestream velocity of 25 m/s with a turbulence intensity of 5%. The incoming boundary layer profile generated over the flat plate is presented in figure 3.

Applying equation 6, the numerical integration of the velocity profile, was used to calculate the boundary layer parameters, δ^* and θ which are defined by equations 3 and 4 for incompressible flows [9]. The shape factor, *H*, was then computed using equation 5 [9].

In equation 6, a and b is the interval, which for the current case spans, i.e., the height of the boundary layer, hence a is 0 and b is δ, divided into several smaller intervals using *i*.

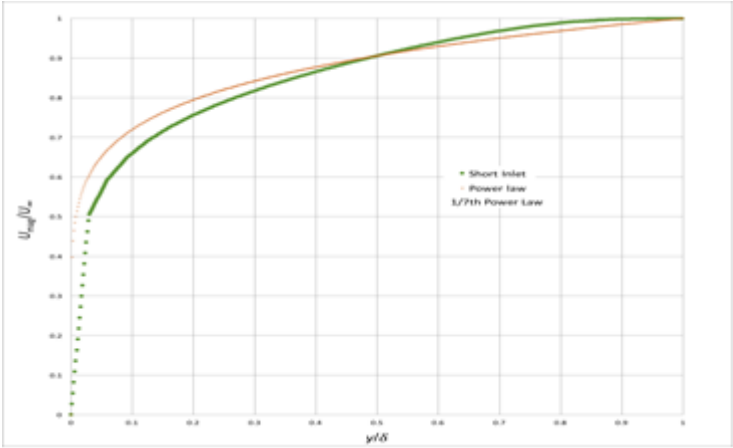

Figure 3. Incoming boundary layer profile

$$\delta^* = \int_0^{\delta} \left(1 - \frac{U(y)}{U_\infty}\right) dy \tag{3}$$

$$\theta = \int_0^{\delta} \frac{U(y)}{U_\infty}\left(1 - \frac{U(y)}{U_\infty}\right) dy \tag{4}$$

$$H = \frac{\delta^*}{\theta} \tag{5}$$

$$\int_a^b f(x)dy \sim \frac{1}{2}\sum_{i=1}^{N}(x_{i+1} - x_i)(f(x_{i+1}) + f(x_i)) \tag{6}$$

From the equations above, i.e. 3, 4, 5, and 6, the following values were obtained for the incoming boundary layer profile over an inlet plate length of 0.4 m.

Boundary layer parameter	Value
δ	10.20 mm
δ^*	1.71 mm
θ	0.93 mm
H	1.82
Re_{Lip}	754,386

Table 2. Boundary layer parameters

2.5. Mesh

A three-dimensional Cartesian, non-uniform, structured mesh is used for all simulations with approximately 2 million cells in the domain. A y^+ of approximately 30 was utilized for the incoming flat plate due to the use of k-ε turbulence model which uses wall functions to model the near wall region, rendering nodes in that region redundant. It also decreases the simulation run time considerably. The nodes are clustered towards the walls and the shear layer region to better capture the high gradients in those areas.

Figure 4 shows the images of the mesh generated for an *L/D* ratio of 16.25 and *L/W* ratio of 8.125 at two different yaw angles to demonstrate the grid and clustering applied. The mesh for a 30^0 yawed cavity can be seen in figure 4d where the mesh nodes in the domain are kept normal to the incoming flow while the cavity is rotated. This leads to a manageable mesh skewness but keeps the mesh cells aligned to the incoming flow and hence improves solution stability.

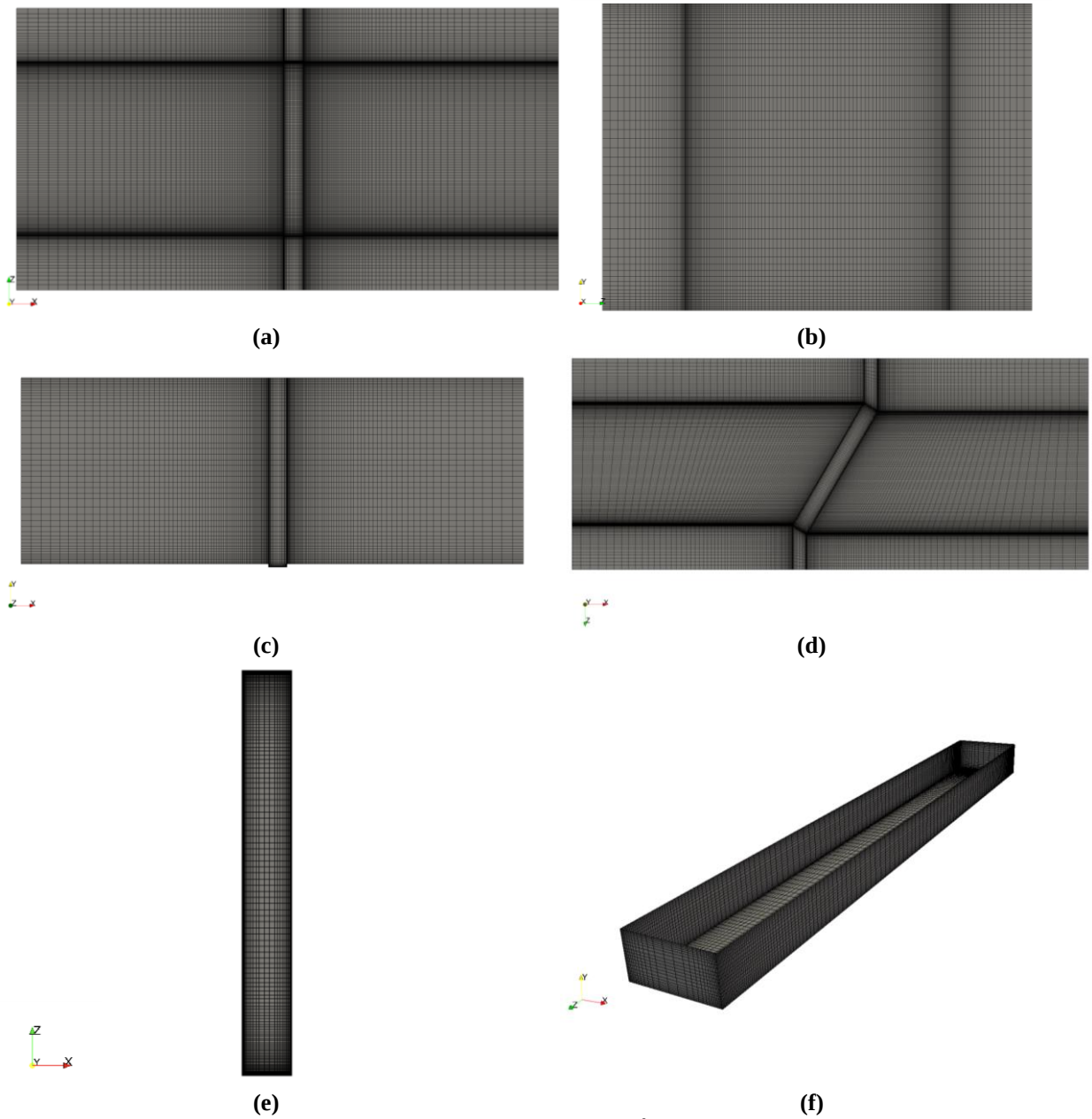

Figure 4. (a). Mesh view, Z axis coming out of the plane, at φ 0^0 (b). Mesh view, Y axis coming out of the plane, at φ 0^0 (c). Mesh on cavity floor, Y axis coming out of the plane, at φ 0^0 (d). Mesh view, Y axis into the plane, at φ 30^0 (e). Mesh on the cavity faces, at φ 0^0

2.6. Turbulence Model:

A standard *k*- ε turbulence model, by Launder and Sharma [14], is used for this investigation, with a freestream turbulent intensity set to 5%. The introduction of two additional transport equations to model the convective and diffusive effects of turbulent energy, makes this two equation model superior over its one equation counter parts. Apart from being a good predictor in the free-stream region, the standard *k*-ε model provided good boundary layer estimates, as can be seen in figure 3.

Two other turbulence models were tested along with the *k*-ε, namely *k*-ω [15] and *k*-ω SST [16], for their supposed [19] accuracy in computing the free shear layer regions. The *k*-ω model is built as a successor for *k*-ε and uses the specific dissipation rate, ω, as the second transport variable. The model is known for its inaccuracy in the freestream region [19]. *k*-ω SST is a hybrid of *k*-ε and *k*-ω which uses *k*-ω in the near wall region and switches to *k*-ε in the free stream. Due to the superior boundary layer prediction and universality, the *k*-ε model was chosen for this study.

III. RESULTS AND DISCUSSION

Pressure contours for two *L/D* ratios are examined below along with the drag profiles for the *L/D* and *L/W* variations mentioned in table 1. The pressure variation on the cavity floor and within the cavity as a whole are presented in figures 5—8. The surface pressure variations provide insight into the effect of geometric and yaw angle variation on the flow physics.

OpenFOAM [17] computes pressure divided by the density term in an incompressible simulation, as shown in equation 7, the resulting pressure term (*P*) is presented as the pressure generated. The pressure discussed in this study is the resultant pressure, *P*.

$$P = \frac{p}{\rho} \tag{7}$$

To further emphasize the pressure variation on the cavity surfaces, the pressure has been locally scaled in figures 5—8.

The pressure distribution on the floor of the cavity with *L/D* of 8.125 and *L/W* of 16.25 is shown in figure 5, while the floor pressure distribution for a cavity with *L/D* of 32.5 and *L/W* of 16.25 is shown in figure 6. The cavities range from shallow to deep and one of each is chosen in the figures below. The cavity floor in figures 5 and 6 are rotated from 0^0 to 90^0 about the Y-axis. The orientation can be understood with the left-hand rule, such that the positive Y-axis goes into the plane of the paper during the counter-clockwise rotation. An accompanying sketch of the cavity orientation is provided in figures 7 and 8 to help clarify the yaw angle at which the pressure contours are presented.

3.1. Effect of Yaw angle on pressure generated:

It can be seen from figures 5a and 5f that the flow transitions from an open-type in 5a at φ 0^0 to a closed type in 5f at φ 90^0, evident due to the pressure stagnation on the cavity floor. In figure 5a, the pressure stagnation is towards the trailing edge of the cavity while it moves further towards the center of the cavity in figure 5f. The velocity streamlines from both these angles make it more evident.

The pressure distribution in figures 5 and 6 also show symmetry when the cavity is aligned to the oncoming flow, in the φ 0^0 and φ 90^0 cases. As the cavity moves through yaw angles from 0^0 to 90^0 the high-pressure region moves along the trailing edge of the cavity floor and the cavity back wall, as can be seen in figures 5, 6, 7 and 8. It can be observed in that there is a higher pressure distribution on the cavity walls turned towards the flow than those turned away from the flow at transitional yaw angles of 30^0, 45^0, 60^0, and 75^0. Shiyani [1] hypothesized that this variation can due to the increasing boundary layer thickness and the resulting energy differential as the flow moves ahead in the positive x direction.

3.2. Effect of *L/D* and *L/W* on pressure generated:

The focus on two *L/D* and *L/W* variations is due to the large amount of pressure data that is gathered during the geometric study. The two sets of pressure data presented show similar trends that can be found in other geometric variations. From figures 5 and 6 on the cavity floors, a similar trend of pressure distribution can be observed for both *L/D* and *L/W* variations with a difference in magnitude. This can be further examined in figures 7 and 8, where the rotation of the cavity leads to the movement of the high-pressure regions from the cavity rear wall to the cavity side walls, as the side walls of the cavity become the rear walls at φ 90^0. This was observed for all the *L/D* and *L/W* variations examined in this investigation. Geometric effects on the pressure profiles showed qualitative change in pressure values, however the effect of geometry produced very little qualitative difference in the pressure distribution. The effect of geometric changes considered is largely quantitative than qualitative. This would further lead to an expected change in drag values due to the pressure magnitude change with different geometries. The pressure stagnation moves along the cavity as the shear layer

impinges on the cavity trailing edge at low yaw angles whilst transitioning to impinging on the cavity flow at high yaw angles.

Based on the *L*, *D* and *W* used in this study, the flow transitions from open type flow at φ 0^0 to a closed type cavity flow at φ 90^0 in all the cases. This is further confirmed by the velocity streamlines in figure 9 and 10, where the 9a and 10a show the shear layer separating of the leading edge and impinging directly on the trailing edge at 0^0 configuration, whereas in figures 9b and 10b, the shear layer separating of the leading edge impinges on the cavity floor after which it reattaches and continues towards the trailing edge at the 90^0 configuration.

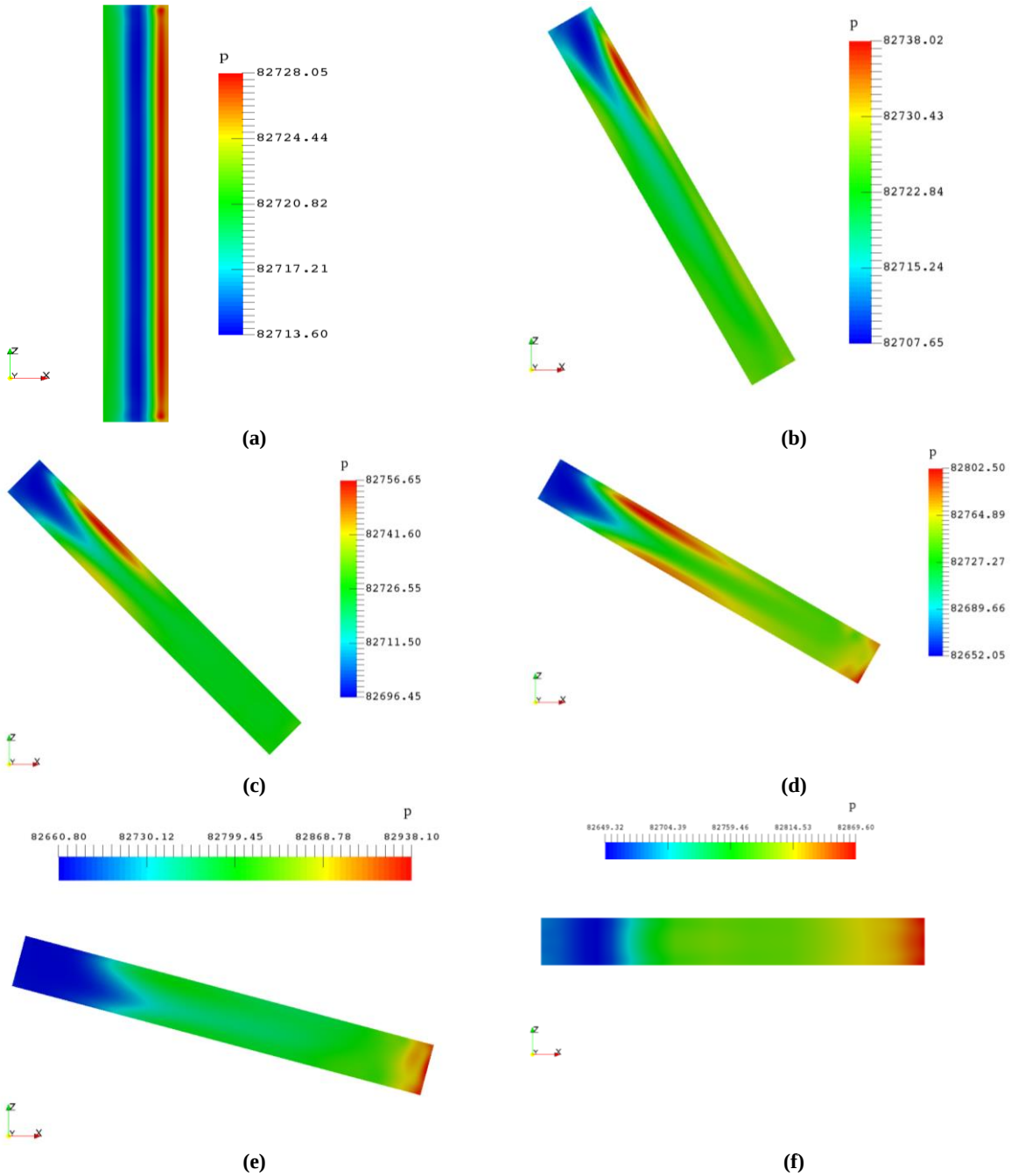

Figure 5. Pressure contours of cavity bottom wall at *L/D*: 8.125, L/W: 16.25 (a) φ 0^0 (b) φ 30^0 (c) φ 45^0 (d) φ 60^0 (e) φ 75^0 (f) φ 90^0

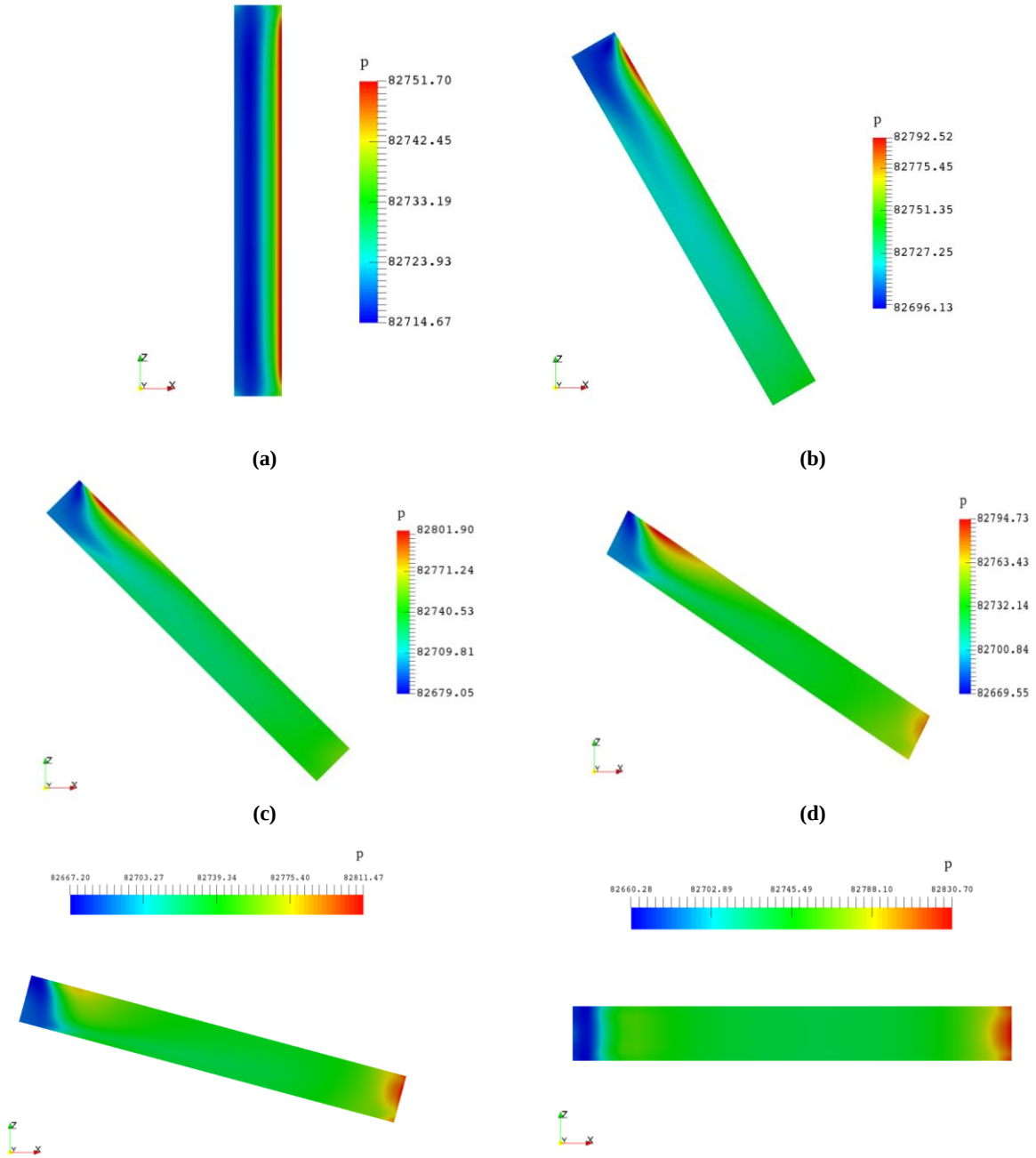

Figure 6. Pressure contours of cavity bottom wall at *L/D*: 32.5, L/W: 16.25 (a) φ 0^0 (b) φ 30^0 (c) φ 45^0 (d) φ 60^0 (e) φ 75^0 (f) φ 90^0

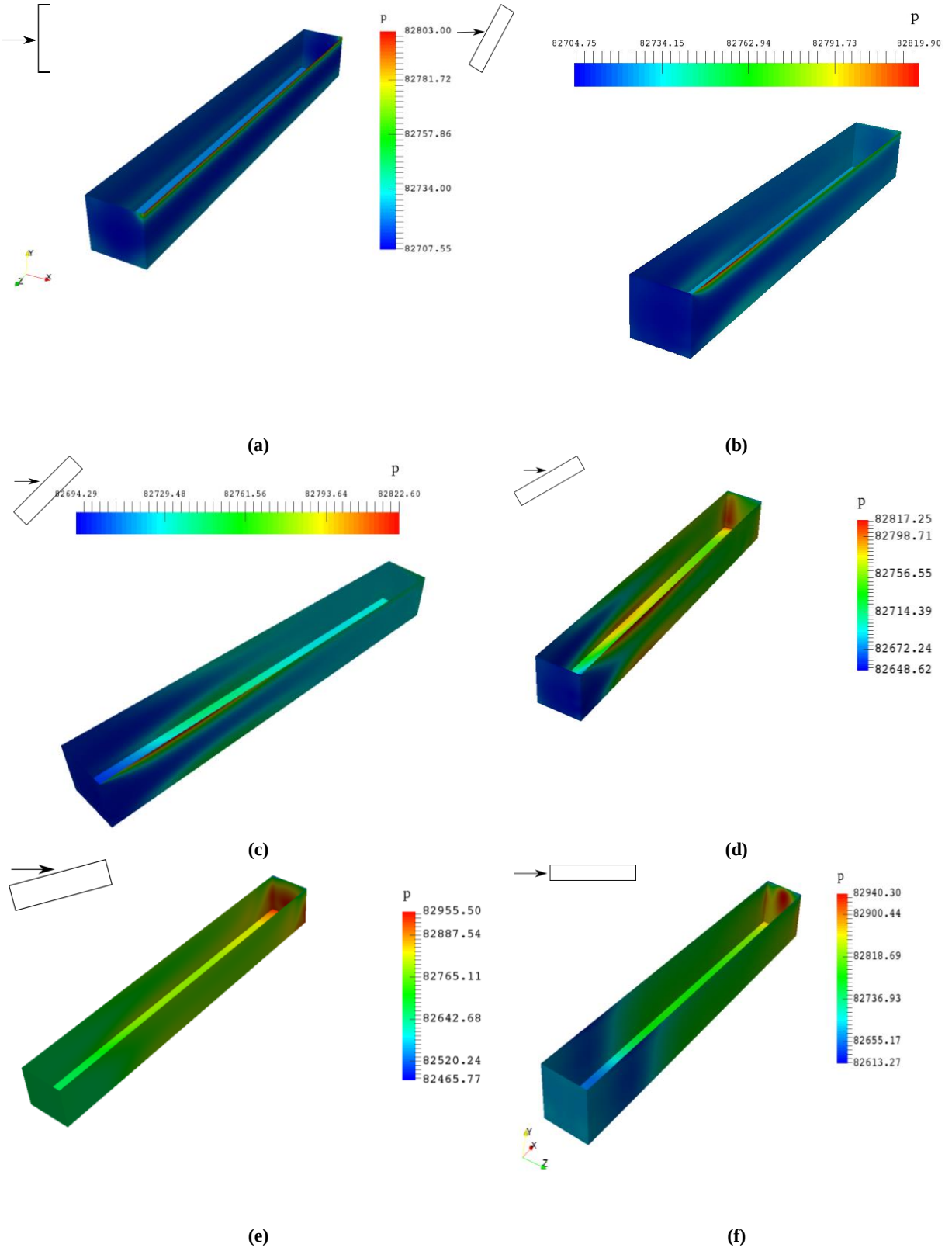

Figure 7. Pressure contours within the cavity, of *L/D*: 8.125, L/W: 16.25, at (a) φ 0^0 (b) φ 30^0 (c) φ 45^0 (d) φ 60^0 (e) φ 75^0 (f) φ 90^0

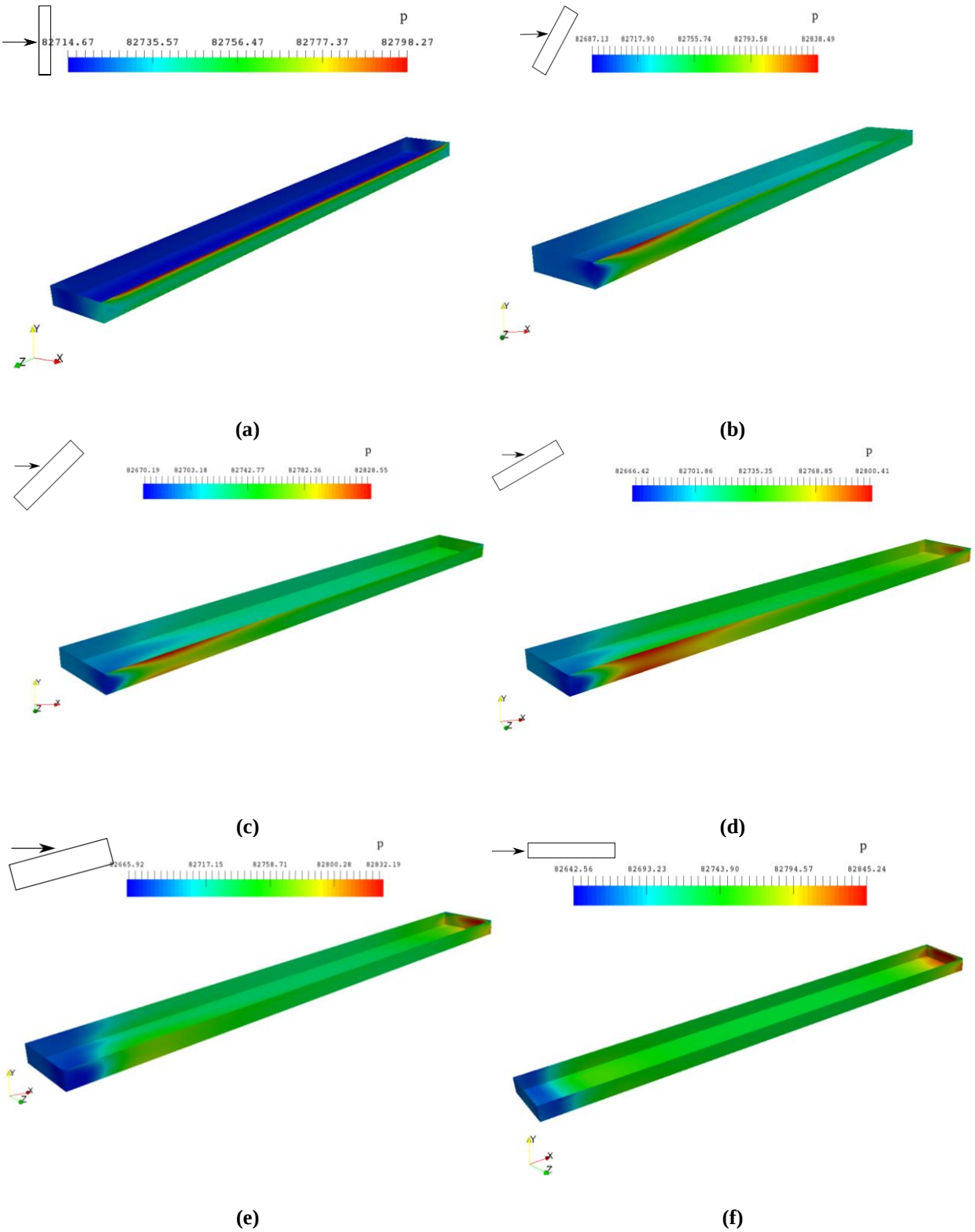

Figure 8. Pressure contours within the cavity, of *L/D*: 32.5, *L/W*: 16.25, at (a) φ 0^0 (b) φ 30^0 (c) φ 45^0 (d) φ 60^0 (e) φ 75^0 (f) φ 90^0

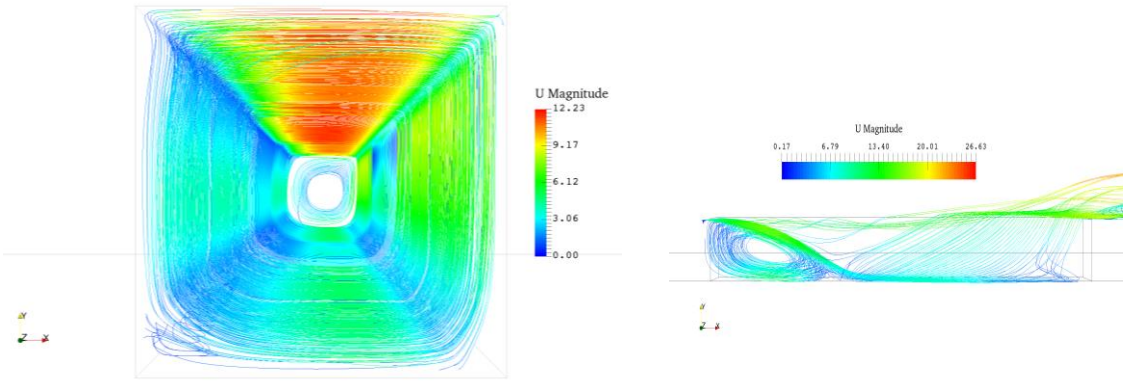

(a) **(b)**

Figure 9. Velocity streamlines within the cavity, of *L/D*: 8.125, *L/W*: 16.25, at (a) φ 0^0 (b) φ 90^0

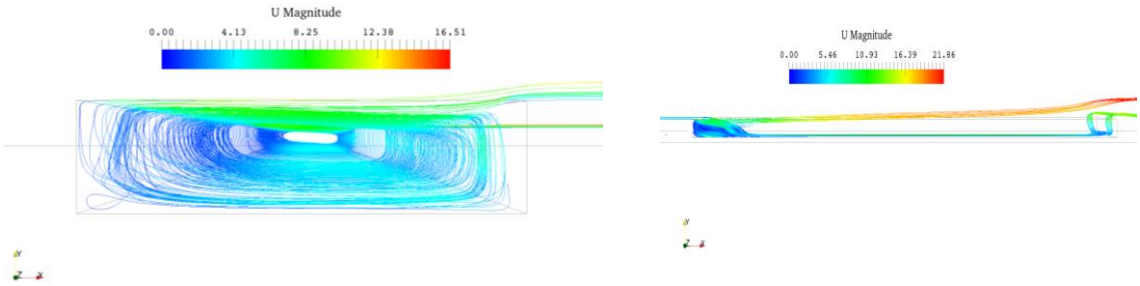

(a) **(b)**

Figure 10. Velocity streamlines within the cavity, of *L/D*: 32.5, *L/W*: 16.25, at (a) φ 0^0 (b) φ 90^0

3.3. Effect of *L/D* and *L/W* on drag:

Figures 11 and 12 present the normalized coefficient of drag, C_d/C_{d_max}, against the yaw angle, φ, for five *L/D* ratio changes in figure 11 and three *L/W* ratio changes in figure 12. The coefficient of drag presented below is a total of both viscous and pressure drag generated on the cavity faces. The drag data was obtained using OpenFOAM's force functions tool, which calculates drag on surfaces.

The effect of *L/D* variation on the drag generated within the cavity shows interesting trends in figure 11. It can be observed that at low *L/D* ratios, *L/D* of 8.125 and *L/D* of 12 in figure 11, the trend follows a bell curve, where the maximum drag peaks at high yaw angles, dropping back again at 900. As the *L/D* ratio is increased the curve starts to flatten out, with the maxima moving towards low yaw angles, *L/D* of 24 in figure 11. After which a transition occurs, where the maximum drag is observed at 0^0 for high *L/D* ratios, namely *L/D* of 32.5 and *L/D* of 65 in figure 11. At these *L/D* ratios, the drag goes down as the yaw angle is increased up until 75^0 after which there is a slight rise in drag in the 90^0 configuration. Though deep and shallow cavities are generally classified with *L/D* ratio of less than 1 and greater than 1 respectively, this transition in the maximum drag w.r.t. yaw angle can be due to the change in cavity type from relatively deep, at low *L/D* ratios, to shallow at high *L/D* ratios. This change suggests that the behavior of drag as a function of yaw angle is highly dependent on the type of cavity. In terms of absolute values, deep cavities have lower drag at low yaw angles, up until 60^0, and should be preferred over shallower cavities in this range. While shallower cavities have lower drag generation at higher yaw angle ranges, above 60^0 compared to its deep counterpart.

Looking at the effect of *L/W* ratios on drag at yaw angles, it can be seen that the fluctuation in qualitative and quantitative values of drag for low ranges of *L/W* ratios, *L/W* of 8.125 and 16.25 in figure 12, is minimal. However, for a very high *L/W* ratio of 65 the behavior changes with a sharp drop in drag values at φ 0^0 and 90^0. At this high *L/W* ratio, the cavity becomes a narrow slit which may be the cause of change in drag behavior. Overall, the effect of change in *L/W* ratios on drag characteristics w.r.t. yaw angles is not very significant for over a large range of *L/W* ratios considered.

For *L/W* variation in figure 12, the maximum drag is observed in higher yaw angles, from approximately 40^0 to 80^0. This supports the notion that the shift in maximum drag from high yaw angles to low yaw angles in the *L/D* ratio study, figure 11, is due to the change in cavity behavior from deep to shallow.

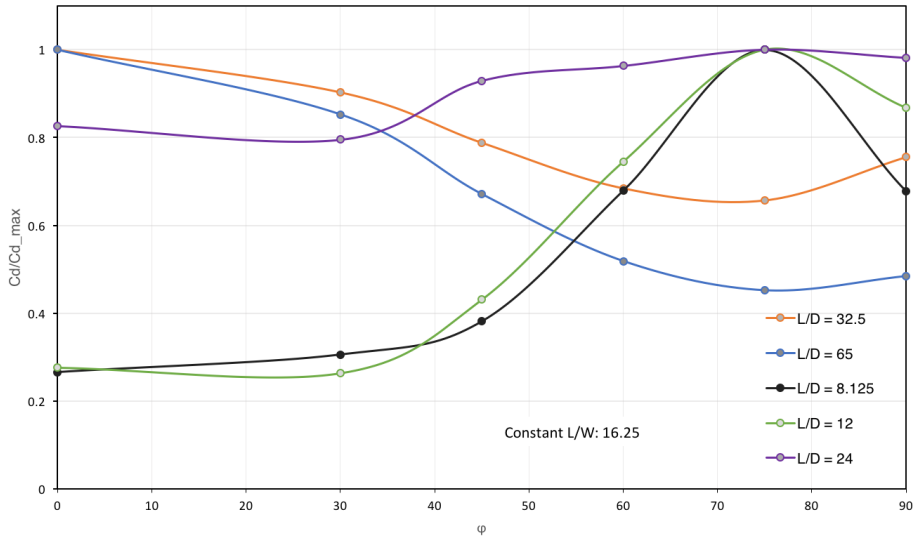

Figure 11. Co-efficient of drag generated within the cavity as a function of yaw angle, for different *L/D* ratios

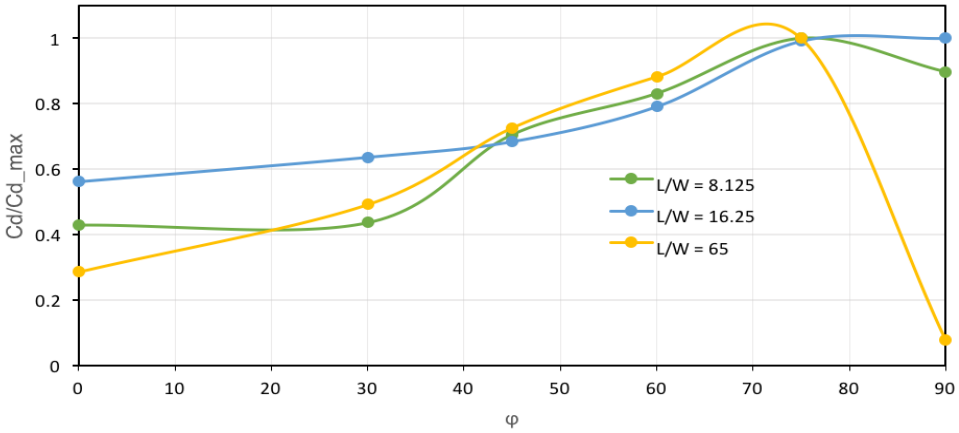

Figure 12. Co-efficient of drag generated within the cavity as a function of yaw angle, for different *L/W* ratios

IV. CONCLUSIONS

The effect of *L/D* and *L/W* ratios on the drag generated by a clean sharp-edged cavity was studied using three-dimensional steady-state simulations with the open-source CFD tool, OpenFOAM. In addition, the effect of yaw angles of 0^0, 30^0, 45^0, 60^0, 75^0, and 90^0, on the drag generated was also examined for each *L/D* and *L/W* ratio variation. A 25 m/s free-stream velocity was used with an atmospheric pressure specified at the outlet.

The pressure profiles on the cavity floor and the cavity as a whole were studied to examine the effect of *L/D*, *L/W* and yaw variation on the cavity pressure distribution. The effect of geometric changes on the cavity pressure distribution was quantitative while qualitatively the pressure profiles were similar. The stagnation and high-pressure regions within the cavity moved as the yaw angle was varied and the effects of three-dimensionality were high when the cavity was yawed w.r.t. the incoming flow. The flow at φ 0^0 and 90^0 exhibited symmetric behavior.

The effect of geometric variations on drag showed interesting trends. For *L/D* variations, the maximum drag shifted from high yaw angles at low *L/D* values to low yaw angles at high *L/D* values. This can be attributed to the cavity flow type moving from deep ranges towards shallow flow. The drag for *L/D* values of 8.125 and 12 drops at 90^0 from a maximum value at 75^0 whereas the drag value for *L/D* of 24 plateaus out with low fluctuations w.r.t φ suggesting a transition region. For *L/D* values above that, i.e. 32.5 and 65, the maximum drag occurs at 0^0 dropping with increase in yaw angle followed by a small rise at φ of 90^0. The effect of *L/W* variation on drag w.r.t. φ was not as pronounced as the effect of *L/D* variation. In the low ranges of *L/W* ratios, the trend lines are very close to each other. When the *L/W* ratio is increased up to 65 there is a qualitative difference in the trend line with sharp drops in drag values at 0^0 and 90^0. However, the maximum drag for all

L/W ratios simulated stays in the higher φ region as opposed to a change in maximum value of drag seen in the *L/D* ratio study, further supporting the hypothesis that the behavior of drag as a function of φ is highly dependent on the type of cavity flow, either deep or shallow.

Further research in this area would yield a more detailed picture of the effect of yawed cavities for the wide range of *L/D* and *L/W* ratios not considered in this study.

REFERENCES

[1]. D. Shiyani, P. J. Disimile, "Effect of yaw angle on drag generated in rectangular cavities," International Journal of Computational Research, vol. 8, pp. 99-113, September 2017.

[2]. K. Weighardt, "Increase in turbulent frictional resistance caused by surface irregularities," Forschungshefte fur Schiffstechnik, vol. 2, pp. 65-81, April 1953.

[3]. I. E. Rossiter, "Wind Tunnel Experiements on the Flow Field over Rectangular cavities at Subsonic and Transonic Speeds," *Aeronautical Research Council*, London, R&M No. 3438, Oct. 1966.

[4]. D. Rockwell and E. Naudascher, "Self-Sustained Oscillations of Impinging Free Sheer Layer," *Annual Review of Fluid Mechanics*, vol. 11, pp. 67-94, 1979.

[5]. S. J. Lawson and G. N. Barakos, "Review of numerical simulations for high-speed, turbulent cavity flows," *Progress in Aerospace Sciences*, vol. 47, pp. 186-216, Feb. 2011.

[6]. ESDU, "Aerodynamics and aero-acoustics of rectangular planform cavities. Part I: time-averaged flow," *Technical Report 02008*, ESDU International; 2004.

[7]. R. L. Stalings, E. B. Plentovich, M. B. Tracy, and M. J. Hemsch, "Measurements of store forces and moments and cavity pressures for a generic store in and near a box cavity at subsonic and transonic speeds," *Technical Report No. NASA-TM-4611*, NASA, 1995.

[8]. X. Gloerfelt, "Cavity Noise," *VKI Lecture: Aerodynamic noise from wall bounded flows*, 2009 Available: http://citeseerx.ist.psu.edu/viewdoc/download?doi=10.1.1.466.1944andrep=rep1andtype=pdf [last-viewed: 16 July 2017]

[9]. F. M. White, *Viscous Fluid Flow, 2nd ed.* McGraw-Hill, New York, 1991, pp. 409 and 413.

[10]. D. Rockwell and E. Naudascher, "Review – Self-Sustaining Oscillations of Flow Past Cavities", *Journals of Fluids Engineering*, vol. 100, June 1978.

[11]. P. J. Disimile, N. Toy, and E. Savory, "Pressure Oscillations in a Subsonic Cavity at Yaw," *AIAA Journal*, Vol. 36, No. 7, July 1998.

[12]. P. J. Disimile, X. Bai, and N. Toy, "Pressure Oscillations within a Yawed Rectangular Cavity in Subsonic Flow," *International Journal of Engineering Research and Industrial Applications (IJERIA)*, Vol. 5, No. II, pp. 27-50, May 2012.

[13]. X. Gloerfelt, C. Bogey, and C. Bailly, "Cavity noise," *Laboratoire de Mécanique des Fluides et d'Acoustique,* Ecole Centrale de Lyon and UMR CNRS 5509, 69134 Ecully, France, Available: https://www.researchgate.net/profile/Xavier_Gloerfelt/publication/226841604_Large_Eddy_Simulations_of_high_Reynolds_number_cavity_flows/links/564471b608aef646e6cae781/Large-Eddy-Simulations-of-high-Reynolds-number-cavity-flows.pdf [last-viewed: 16 July 2017]

[14]. B. E. Launder and B. I. Sharma, "Application of the Energy Dissipation Model of Turbulence to the Calculation of Flow Near a Spinning Disc," *Letters in Heat and Mass Transfer*, vol. 1, no. 2, pp. 131-138, 1974.

[15]. D. Wilcox, "Re-assessment of the scale-determining equation for advanced turbulence models," *AIAA Journal*, vol. 26, no. 11, pp. 1299-1310, 1988.

[16]. F. R. Menter, "Two-Equation Eddy-Viscosity Turbulence Models for Engineering Applications," *AIAA Journal*, vol. 32, no. 8, pp. 1598-1605, 1994.

[17]. The OpenFOAM Foundation, "OpenFOAM – User Guide 4.0," June 2016, Available: http://foam.sourceforge.net/docs/Guides-a4/OpenFOAMUserGuide-A4.pdf [last-viewed: 16 July 2017]

[18]. Krishnamurty, K. 1956 Sound radiation from surface cutouts in high speed flow. PhD thesis, California Institute of Technology.

[19]. Ferziger, J. H.; Peric, M. (2001), "Computational Methods for Fluid Dynamics", Springer-Verlag. ISBN 978-3-540-42074-3.

Dhaval Shiyani1 "Study of Geometric Variations on Drag over Rectangular Cavities at Yaw" International Journal of Computational Engineering Research (IJCER), vol. 08, no. 02, 2018, pp. 06–18.